CJC Chinese Journal of Chemistry
中 国 化 学 - An International Journal

For submission: https://wiley.atyponrex.com/journal/CJOC
For published articles: https://onlinelibrary.wiley.com/journal/16147065

Cite this paper: *Chin. J. Chem.* **2025**, *43*, 2120—2128. **DOI: 10.1002/cjoc.70075**

Non-Halogenated Solvent Processed Ternary All-Polymer Solar Cell with PCE of 18.55% Enabled by Two Compatible Polymer Acceptors[†]

Rouren Chen,[‡,a] Tianyi Zhang,[‡,a] Qiqing Ruan,[a] Lunbi Wu,[b] Zhixuan Xu,[a] Yuan Su,[a] Zhixiong Cao,[c] Qingduan Li,*[,a] Biao Xiao,[d] Ruijie Ma,*[,e] Yue-Peng Cai,[a] Tao Jia,*[,b] Shengjian Liu,*[,a] and Gang Li[e]

[a] *School of Chemistry, Guangzhou Key Laboratory of Materials for Energy Conversion and Storage, Guangdong Provincial Engineering Technology Research Center for Materials for Energy Conversion and Storage, South China Normal University (SCNU), Guangzhou, Guangdong 510006, China*
[b] *School of Optoelectronic Engineering, Guangdong Polytechnic Normal University, Guangzhou, Guangdong 510665, China*
[c] *School of Medical Information Engineering, Gannan Medical University, Ganzhou, Jiangxi 341000, China*
[d] *Key Laboratory of Optoelectronic Chemical Materials and Devices (Ministry of Education), Flexible Display Materials and Technology Co-Innovation Centre of Hubei Province, School of Optoelectronic Materials & Technology, Jianghan University, Wuhan, Hubei 430056, China*
[e] *Department of Electrical and Electronic Engineering, Research Institute for Smart Energy (RISE), Photonic Research Institute (PRI), Guangdong-Hong Kong-Macao Joint Laboratory for Photonic-Thermal-Electrical Energy Materials and Devices, The Hong Kong Polytechnic University, Hong Kong, China*

Keywords

All-polymer solar cells | Power conversion efficiency | Ternary construction | Guest selection | Polymer acceptors | Nonradiative recombination

Comprehensive Summary

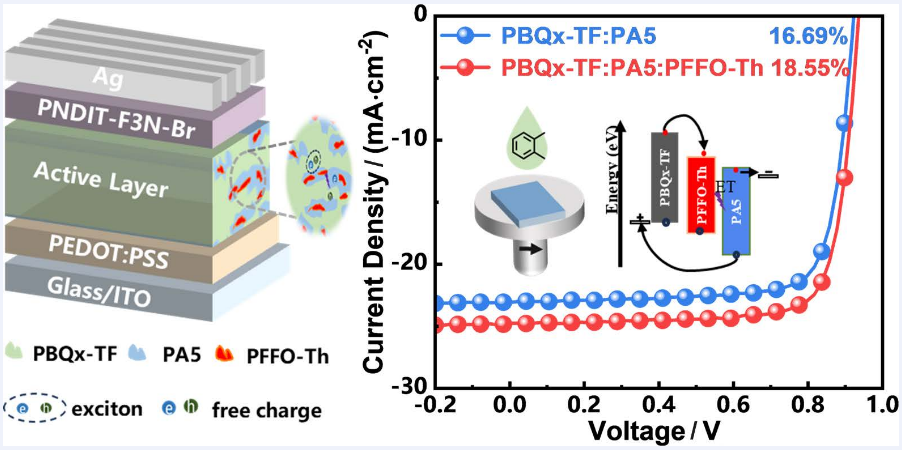

Herein, a theory-guided ternary construction case on boosting power conversion efficiency (PCE) for all-polymer solar cell (all-PSC) is reported, where guest acceptor's characteristics include high miscibility with host polymer acceptor, significantly larger optical band-gap, and improved luminescence. Consequently, with only 10 wt% PFFO-Th (third component) addition, the PCE of binary control is promoted to 18.55% from 16.69%, a 11.1% relative increase, demonstrating the great effectiveness of this ternary strategy. Besides, the realized 18.55% efficiency is at state-of-the-art level of all-PSCs processed by *ortho*-xylene, a widely acknowledged green non-halogenated solvent by the field. This study shares new thought on designing high-performance photovoltaic devices with reduced energy losses and favorable charge dynamics, which would nourish future development on all-PSCs, and even other organic electronics.

---

*E-mail: qingduan.li@m.scnu.edu.cn; ruijie.ma@polyu.edu.hk; tjia@gpnu.edu.cn; shengjian.liu@m.scnu.edu.cn

[‡] These authors contributed equally.

[†] Dedicated to the Special Issue of Emerging Investigators in 2025.

Background and Originality Content

While the power conversion efficiency (PCE) of all-polymer solar cell (all-PSC) has been promoted to an unprecedented level, thanks to the emergence of the polymerized small molecular acceptor (PSMA) and corresponding donor polymers,[1-18] their absolute performance still cannot appeal with small molecular acceptor-based counterparts, which have surpassed 20% on PCE values, thanks to not only material innovation, but also the various combinations on ternary blend construction.[19-34] Therefore, to further improve the development of all-PSCs, whose thermally stable and mechanical robust properties are intrinsically appreciated,[35] pursuing the PCE via effective and representative ternary strategy is of great significance.

Empirically, the efficiency enhancement of ternary blend relies on selecting guest component with larger bandgap and high miscibility, as well as similar charge transfer (CT) state and high external quantum efficiency of electroluminescence (EQE-EL).[36] To date, there's few cases in ternary all-PSCs satisfying these standards, which results in limited efficiency enhancement.[37-40] Theoretically, assuring the third component that fulfills all above requirements, without significant incorporation ratio, the efficiency of ternary system would also be distinguishably promoted.

Herein, we introduce an uncommonly concentrated wide bandgap PSMA, named PFFO-Th into the high-efficiency host blend PBQx-TF:PA5, to study the theory guided strategy's effectiveness.[41-43] Compared to low bandgap acceptor PA5, PFFO-Th shows a significantly larger bandgap, highly compatible miscibility, as well as increased EQE-EL, enabling it a well suitable guest component in ternary construction. Specifically, this work demonstrates a theory-guided design where PFFO-Th simultaneously fulfills three critical roles: (1) a miscibility mediator between polymer acceptors, (2) a luminescence enhancer, and (3) a crystallinity modulator. Consequently, with 10% weight ratio incorporation of PFFO-Th, the device efficiency is promoted to 18.55% from binary control's 16.69%, demonstrating a 11.1% relative improvement. In addition, 18.55% is also a value appealing state-of-the-art all-PSCs cast by o-XY, a widely acknowledged green non-halogenated solvent in the field. Parallelly, a series of characterizations prove that 10 wt% PFFO-Th can effectively modulate the crystalline features, towards suppressed carrier recombination and boosted charge transport, which responds to optimized short-circuit current density (JSC) and fill factor (FF). Our work presents not only high-performance on non-halogenated solvent processed all-PSC, but also a valuable case confirming the effectiveness of guest component selection, which could be more than useful for further development on all-PSC and even organic solar cells field.

Results and Discussion

The chemical structures of the polymer donor PBQx-TF and polymer acceptors PA5, PFFO-Th are shown in Figure 1a. The electronic characteristics of PBQx-TF PA5, and PFFO-Th (Figure S1, Supporting Information) were examined through cyclic voltammetry (CV) measurements. This electrochemical analysis enabled the determination of both the highest occupied molecular orbital (HOMO) and lowest unoccupied molecular orbital (LUMO) energy levels. The HOMO and LUMO levels of PBQx-TF were measured to be −5.48 eV and −3.58 eV, respectively (Figure 1b). The deep HOMO level of PBQx-TF is advantageous for achieving a high V_{OC} in solar cell devices. For the polymer acceptors, PFFO-Th and PA5 exhibited HOMO/LUMO energy levels of −5.66/−3.71 eV and −5.72/−3.78 eV, respectively, demonstrating good energy level alignment with PBQx-TF. Importantly, PFFO-Th acts as an energy level adjuster, forming a LUMO energy level gradient among the three materials. This energy level architecture is expected to facilitate efficient exciton dissociation at the PBQx-TF/PFFO-Th/PA5 interface, as will be corroborated by subsequent tests. Figure 1c illustrates the absorption profiles of the pristine polymer components. The polymer donor PBQx-TF displayed dual absorption bands at 543 nm (lower intensity) and 576 nm (higher intensity), corresponding to 0-1 and 0-0 vibrational transitions, respectively, which refer to 0-1 vibrational peak and 0-0 vibrational peak, respectively. While the polymer acceptors PA5 and PFFO-Th show absorption peaks at 690 nm and 615 nm, respectively. The complementary absorption ranges of the polymer acceptors align well with that of the polymer donor, broadening the overall light-harvesting capability of the blend. This spectral complementarity is crucial for enhancing photocurrent generation in the device.

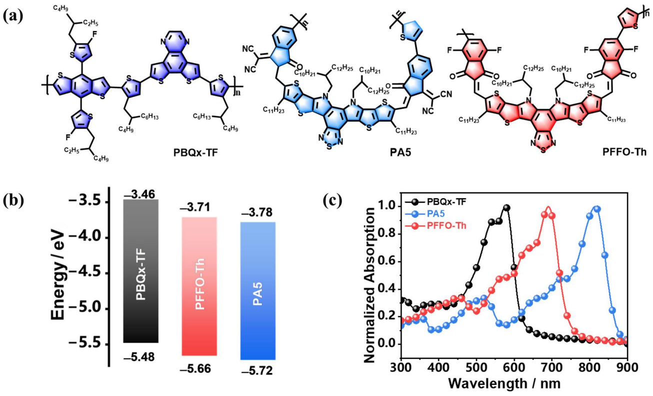

Figure 1 (a) Chemical structures of PBQx-TF, PA5, PFFO-Th. (b) Normalized absorption spectra of PBQx-TF, PA5,PFFO-Th based films. (c) Energy level structure of the active layer materials.

The molecular packing characteristics of the neat polymers were analyzed using grazing-incidence wide-angle X-ray scattering (GIWAXS). Figure S2 illustrates the 2D color patterns of PBQx-TF, PA5, and PFFO-Th films. Both PBQx-TF and the acceptors PA5 and PFFO-Th demonstrated a favorable face-on orientation, with distinct in-plane (IP) lamellar and out-of-plane (OOP) π–π stacking peaks. The PA5 acceptor exhibited higher overall crystallinity compared to PFFO-Th, suggesting that increasing the PFFO-Th content in the acceptor blend films might reduce crystallinity and orientation. Furthermore, the π–π peaks of PBQx-TF and the two acceptor molecules are located in close proximity, which implies that their blending could enhance film crystallinity, with additional PFFO-Th potentially serving as a regulator.

The absorption properties of BHJ active layers were also investigate as shown in Figure S3 in Supporting Information. In contrast to the neat films, PBQx-TF showed stronger vibrational peaks for the 0-1 transition than for the 0-0 types. Since H-aggregation enlarges the bandgap while J-aggregation narrows it, we can identify enhanced H-aggregation by observing a rise in the 0-1 vibrational peak and a decrease in the 0-0 vibrational peak. Additionally, the absorption profiles of blend films in the range of 750—900 nm closely resembled PA5 film. These observations suggest that PBQx-TF had minimal influence on the overall aggregation behavior of PA5 while the aggregation of the donor material was notably influenced by the addition of PFFO-Th.

To evaluate the performance of the all-polymer solar cells, devices were fabricated with the standard ITO/PEDOT:PSS/active layer/PNDIT-F3N-Br/Ag architecture. The resulting current density-voltage (*J-V*) characteristics and performance parameters, are summarized in Figure 2a and Table 1. The binary all-PSC based on PBQx-TF:PA5 achieved a PCE of 16.69%, with a V_{OC} of 0.91 V, a J_{SC} of 23.36 mA·cm^{-2}, and an FF of 78.27%. As a result of the mismatch of energy level and absorption spectra, binary devices of PBQx-TF:PFFO-Th showed a low PCE of 8.55%, with a high V_{OC} of 1.44 V and low J_{SC} and FF of 12.99 mA·cm^{-2} and 45.76%, respectively. In comparison, the addition of 10% PFFO-Th to the PBQx-TF:PA5 system significantly enhanced the photovoltaic performance. The optimized ternary all-PSC reached a PCE of 18.55%, with a V_{OC} of 0.94 V, a J_{SC} of 24.95 mA·cm^{-2}, and an FF of 79.11%. Conclusion of device performance with other content ratios of PFFO-Th and other optimized conditions are provided in Supporting Information (Tables S1—S5). The external quantum efficiency (EQE) spectra of the devices, shown in Figure 2b, confirm the improved performance of the ternary blend. The integrated J_{SC} values from the EQE measurements are 23.17 mA·cm^{-2} for the PBQx-TF:PA5 device and 23.77 mA·cm^{-2} for the PBQx-TF:PA5:PFFO-Th device, respectively, align well with the *J-V* results, within a reasonable error margin of ~5%. The addition of PFFO-Th resulted in a ~10% improvement in the PCE compared to the binary PBQx-TF:PA5 system. This enhancement is attributed to the significant increase in J_{SC}, which is directly reflected in the broader and higher EQE response observed across the 450—850 nm wavelength range. The improved light absorption and charge transport properties provided by the ternary blend are critical factors driving this performance boost. The device reproducibility was evaluated across 10 devices, with the calculated mean and standard deviation for the photovoltaic parameters demonstrating good consistency. This robust reproducibility highlights the reliability of the resultant ternary system for practical applications. As shown in Table S6, the statistics of a direct comparison of ternary all-PSCs devices of our new and other results reported in recent years was performed. It could be seen that our result, especially compared to those with non-halogenated solvents, is among the highest ones.

Morphological characterization

To better understand how PFFO-Th, as the third component in the PBQx-TF:PA5 system, influences molecular crystallinity, compatibility, and morphology, we performed a series of characterizations, including atomic force microscopy (AFM, Figure 3a, transmission electron microscopy (TEM, Figure 3b) and contact angle (CA) measurement (Figure S4 and Table S7, Supporting Information).[44-46] The surface energies (γ) of PBQx-TF, PA5, and PFFO-Th were estimated to be 24.00, 36.30, and 35.95 mJ·m^{-2}, respectively. Using the Flory-Huggins theory, we calculated the Flory-Huggins parameter χ by the equation $\chi = K(\sqrt{\gamma_1} - \sqrt{\gamma_2})^2$ (where, K is a proportionality constant, γ_1 and γ_2 are the surface energies of the two components), χ values of 1.2778 K between PBQx-TF and PA5 and 1.2034 K between PBQx-TF and PFFO-Th were obtained. The higher χ value indicates lower miscibility between PBQx-TF and PFFO-Th, promoting phase separation during film deposition. Conversely, the smaller χ value of 0.0291 K between PA5 and PFFO-Th suggests good miscibility, which is critical for optimizing blend morphology.

Table 1 Summary of device parameters of the optimized PSCs

Active layer PBQx-TF:PA5:PFFO-Th	V_{OC}/V	J_{SC}/ (mA·cm^{-2})	FF/%	PCE/%	PCE^a/%
1:1:0	0.91	23.36	78.27	16.69	16.59±0.28
1:0.9:0.1	0.94	24.95	79.11	18.55	18.32±0.29
1:0:1	1.44	12.99	45.76	8.75	8.55±0.31

^{a} Average PCEs are obtained from more than 10 devices.

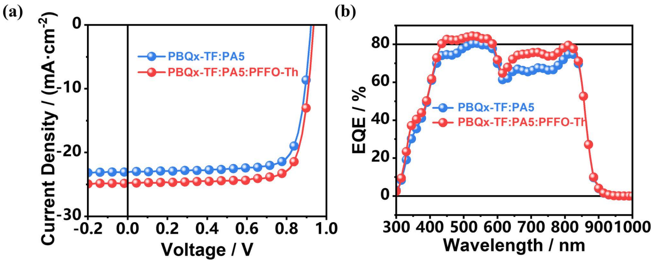

Figure 2 (a) *J-V* curves of all-PSCs based on PBQx-TF:PA5 and PBQx-TF:PA5:PFFO-Th. (b) EQE spectra for PBQx-TF:PA5 and PBQx-TF:PA5:PFFO-Th based all-PSC devices.

According to the AFM and TEM results, all blend films displayed a fibril-like surface structure, facilitating efficient charge generation. As previously mentioned, PBQx-TF demonstrated relatively good miscibility with PFFO-Th. The PBQx-TF:PA5 film showed a root-mean-square roughness (RMS) of 1.75 nm. The increased RMS observed in films with 10% PFFO-Th may result from enhanced crystallinity, which improves charge transport and aligns with the higher mobility observed. Thin fibrils with diverse lengths were observed in both the AFM and TEM images. Although, the RMS was increased slightly by 0.02 nm compared to that of PBQx-TF:PA5 binary blend, the elongated fibrils created pathways for efficient charge transport and lowered trap densities, leading to enhanced device performance. These fibril-like regions, consisting of pure phases, likely contributed to reduced exciton recombination. This phenomenon may arise from the strong

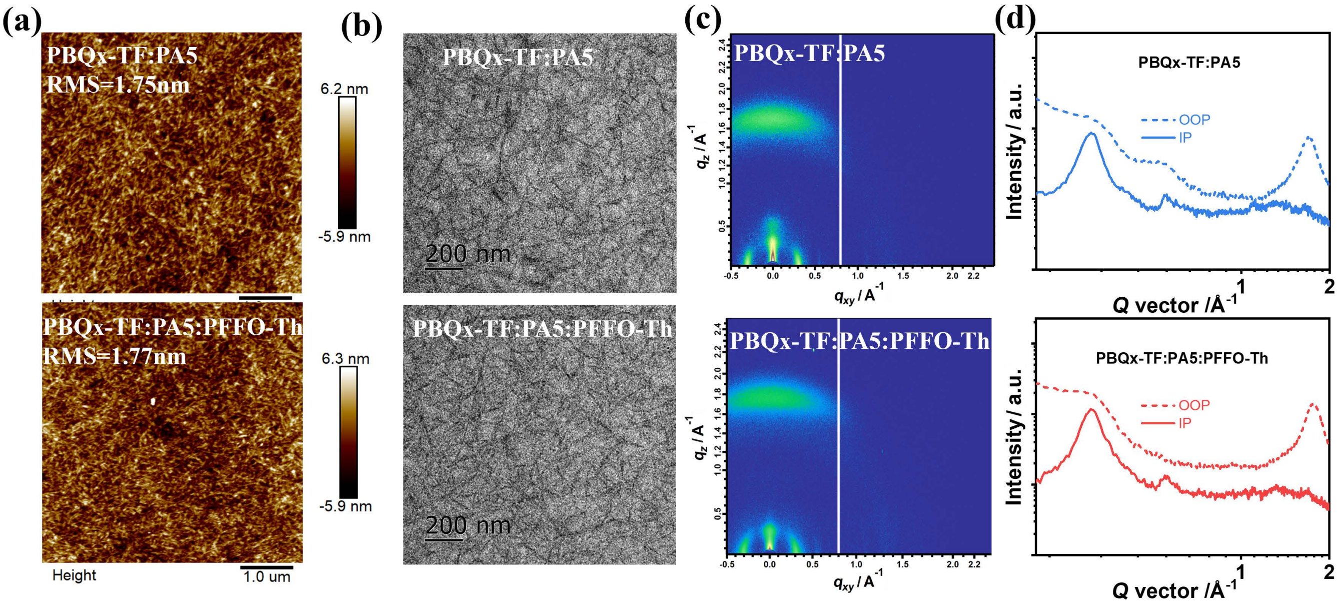

Figure 3 (a) AFM height images of binary and ternary films. (b) TEM images for binary and ternary films. (c) 2D-GIWAXS patterns of binary and ternary films. (d) Line-cut profiles derived from Figure 3c.

H-aggregation behavior of PBQx-TF in the blends.

To explore the influence of PFFO-Th incorporation on the crystallographic arrangement and molecular alignment within the active layer via a larger spatial view, we performed GIWAXS tests on PBQx-TF:PA5 and PBQx-TF:PA5:PFFO-Th films.[47-50] As depicted in Figure 4d, GIWAXS analysis revealed that the PBQx-TF:PA5:PFFO-Th ternary film exhibits a lamellar stacking peak at q = 0.31 $Å^{-1}$ (interlamellar spacing d = 20.43 Å) in the in–plane (IP) direction, demonstrating tighter molecular packing compared to the binary PBQx-TF:PA5 system (q = 0.30 $Å^{-1}$, d = 21.20 Å). This structural compression highlights the role of PFFO-Th in optimizing active-layer crystallinity. The detailed information and relevant crystallographic parameters derived from the line-cut profiles are shown in Figure 3e and Tables S8—9. The crystal domain size is evaluated by the crystal coherence length (CCL), which is calculated from Scherrer equation: CCL = 2πk/FWHM, where FWHM is the full-width at half-maximum of the peak of crystallization and k denotes a constant, here adopted as 0.9. The CCLs of the π–π stacking peak (OOP direction) and lamellar stacking peak (IP direction) for PBQx-TF:PA5–based film are 29.50 Å and 152.30 Å, respectively, and the CCLs in the OOP direction and IP direction for PBQx-TF:PA5:PFFO-Th based film are 30.46 Å and 157.57 Å, respectively. It is important to note that coherence length values can only represent crystalline orderliness, while crystallinity should be correlated with diffraction intensity, the latter being replaced by peak area.[50] The introduction of PFFO-Th induces a 0.77 Å reduction in lamellar spacing (from 21.20 Å to 20.43 Å), as evidenced by the GIWAXS-derived q-shift in the IP direction, confirming its role in enhancing molecular packing density within the ternary active layer. The simultaneous increase in both coherence length (ordering) and diffraction intensity (crystallinity) follows classical polymer crystallization theory, where the low χ parameter (0.029 K) between PA5/PFFO-Th enables cooperative crystallization. This dual improvement in crystalline quality–quantitatively confirmed by peak area analysis–directly enhances charge transport. The improved face-on orientation and tighter π-π stacking induced by PFFO-Th facilitate vertical charge transport while the increased crystal coherence length reduces grain boundary recombination. These structural enhancements correlate directly with the observed improvements in charge mobility and device performance. These structural and electronic improvements directly correlate with the observed increases in J_{SC} and FF.

To evaluate the influence of PFFO-Th on exciton dissociation efficiency and charge collection dynamics, we analyzed the photocurrent density (J_{ph}) as a function of effective voltage (V_{eff}) for the fabricated devices. Here, J_{ph} is expressed as the difference between the J_{light} and J_{dark}, which represent the current densities measured under illuminated and dark conditions, respectively. V_{eff} is given by $V_{eff} = V_{bi} - V_{appl}$, where V_{bi} represents the voltage at which J_{ph} equals zero, and V_{appl} stands for applied voltage. The J_{ph}s achieved saturation before the V_{eff} region at 2.0 V, suggesting that the internal electric field is sufficiently strong to effectively sweep out all charge carriers. The $P(E,T)$ is calculated as the ratio of J_{ph} to $J_{ph,sat}$, where J_{ph} represents the current density under short-circuit conditions, and $J_{ph,sat}$ corresponds to the saturated current density. As derived from Figure 4a, the $P(E,T)$ value of the PBQx-TF:PA5:PFFO-Th ternary all-PSC (98.88%) exceeds that of the PBQx-TF:PA5 binary all-PSC (96.30%), indicating enhanced exciton dissociation efficiency. This improvement contributes to higher J_{SC} and FF performance.

The charge recombination behavior was also performed. As illustrated in Figure 4b, the J_{SC} and V_{OC} values derived from J-V curves under different light intensity are plotted as functions of light intensity (P_{light}). The relationship between J_{SC} and P_{light} follows a power-law dependence, $J_{SC} \sim P_{light}{}^{\alpha}$, where the exponent α reflects the extent of bimolecular recombination. When α approaches 1, the active layer demonstrates optimized charge transport dynamics and minimal bimolecular recombination losses. For the ternary device, the optimized α reached 0.97, surpassing the value of 0.96 for the PBQx-TF:PA5 binary device, demonstrating effective suppression of bimolecular recombination. Additionally, geminate recombination loss can be evaluated by analyzing the relationship between V_{OC} and P_{light}. The slope of the semi-log plot of V_{OC} versus Plight is determined using the formula kT/q, where k represents Boltzmann's constant, T is the temperature in Kelvin, and q is the elementary charge. A slope equal to kT/q indicates dominant bimolecular recombination, while deviations suggest the prevalence of monomolecular or trap-assisted recombination mechanisms. Trap-assisted recombination is significantly reduced when the ideality factor (n) approaches 1, whereas values close to 2 indicate nearly complete charge recombination. Based on the linear fitting in Figure 4c, the n values were determined to be 1.07 for the PBQx-TF:PA5 binary devices. In contrast, the ternary PBQx-TF:PA5:PFFO-Th device exhibited a lower n value of 1.02, indicating effective suppression of trap-assisted recombination. The suppression of both types of recombination mechanisms leads to enhanced charge transport and extraction efficiency, directly contributing to the observed improvements in J_{SC} and FF in the ternary devices. The improved device performance in the PBQx-TF:PA5:PFFO-Th ternary system is attributed to a synergistic relationship between morphology and charge dynamics. The addition of PFFO-Th induces favorable phase separation, enhances crystallinity, and optimizes molecular stacking. These structural modifications lead to i) improved energy transfer pathways and increased dissociation probability; ii) suppression of both bimolecular and trap-assisted recombination; iii) formation of transport channels through PFFO-Th, facilitating reduced trap density and higher mobility.

To investigate the working mechanism of the ternary all-PSC,

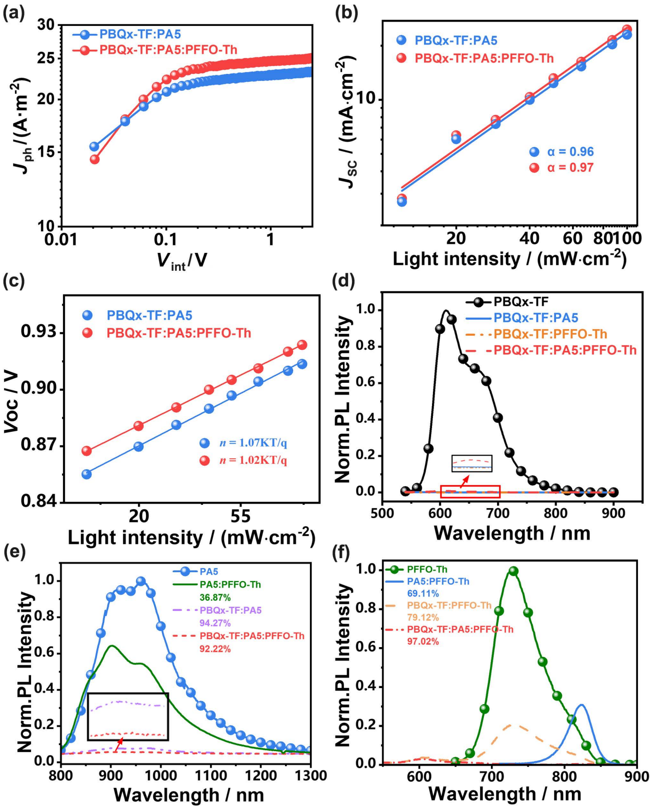

Figure 4 (a) The J_{ph}-V_{eff} curves of the all-PSCs. (b) V_{OC}-Plight curves of the all-PSCs. (c) J_{SC}-P_{light} curves of the all-PSCs. (d) PL spectra of pristine donor and PBQx-TF:PA5, PBQx-TF:PFFO-Th, PBQx-TF:PA5:PFFO-Th blended films excited at 530 nm. (e) PL spectra of PA5 and PBQx-TF:PA5, PA5:PFFO-Th, PBQx-TF:PA5; PFFO-Th blended films excited at 780 nm. (f) PL spectra of PFFO-Th and PA5:PFFO-Th, PBQx-TF:PFFO-Th blended films excited at 580 nm.

steady-state photoluminescence (PL) spectroscopy was performed.[51] As illustrated in Figure 4d, the primary emission peak of the PBQx-TF neat film appears at 600 nm under 530 nm excitation, with quenching efficiency reaching up to 99% in both binary and ternary devices. This indicates that the donor emission is nearly entirely quenched by the introduction of PFFO-Th, as shown in Figures 4d—f, shows that there is an energy transfer between PFFO-Th and PBQx-TF, and the addition of PFFO-Th promotes the exciton dissociation. Moreover, the overlap between the absorption spectrum of PA5 and the PL emission of PFFO-Th indicates the presence of Förster resonance energy transfer (FRET) from PFFO-Th to PA5. FRET is a non-radiative energy transfer mechanism where an excited molecule transfers its energy to a nearby molecule through dipole-dipole coupling. For FRET to occur efficiently, the following conditions must be met: First, the photoluminescence (PL) emission spectrum of the donor molecule must overlap with the absorption spectrum of the acceptor. Second, the donor and acceptor should be within the Förster radius (~ a few nm) for effective coupling. Third, the transition dipoles of the donor and acceptor should be favorably oriented. The overlap between the absorption spectrum of PA5 and the PL emission of PFFO-Th indicates the presence of FRET from PFFO-Th to PA5. In this system, PFFO-Th acts as the donor, and PA5 acts as the acceptor. The spectral overlap between the emission of PFFO-Th and the absorption of PA5 facilitates the energy transfer process, allowing excitons to move from PFFO-Th to PA5. This mechanism facilitates exciton transport, improving both dissociation and charge transfer. Thus, the incorporation of PFFO-Th not only enhances exciton dissociation but also provides additional transport pathways, effectively reducing recombination losses.

Transient photocurrent (TPC) measurements were employed to elucidate the impact of PFFO-Th on charge extraction processes in polymer solar cells (PSCs), providing insights into its role in enhancing device performance. The data from TPC measurements (Figure 5a) indicate that devices with 10% PFFO-Th exhibit a charge extraction time of 0.17 µs, which is shorter than the 0.24 µs observed for devices without PFFO-Th. These findings suggest that incorporating 10% PFFO-Th enhances charge transfer efficiency, aligning with the corresponding reduced recombination and higher J_{SC}. Additionally, the electron (μ_e) and hole (μ_h) mobilities of the devices were determined using the space-charge-limited current (SCLC) method, with the results presented in Figure 5b and Table S10 (Supporting Information). A μ_h/μ_e ratio closer to 1 indicates more balanced charge transport within active layers. For the PBQx-TF:PA5 blends, the calculated μ_h and μ_e values were 1.78×10^{-3} $cm^2 \cdot V^{-1} \cdot s^{-1}$ and 7.8×10^{-4} $cm^2 \cdot V^{-1} \cdot s^{-1}$, respectively, yielding a ratio of 2.29. When 10 wt% of PBQx-TF was added to the PBQx-TF:PA5 blends, the μ_e value increased to 2.57×10^{-3} $cm^2 \cdot V^{-1} \cdot s^{-1}$, while the μ_h decreased to 3.32×10^{-3} $cm^2 \cdot V^{-1} \cdot s^{-1}$, resulting in a decreased ratio of 1.29. The reduced μ_h/μ_e ratio suggests superior charge transport in the ternary devices. The enhanced electron mobility and improved charge balance can lower the probability of charge recombination, contributing to higher FF and J_{SC} for the ternary device.

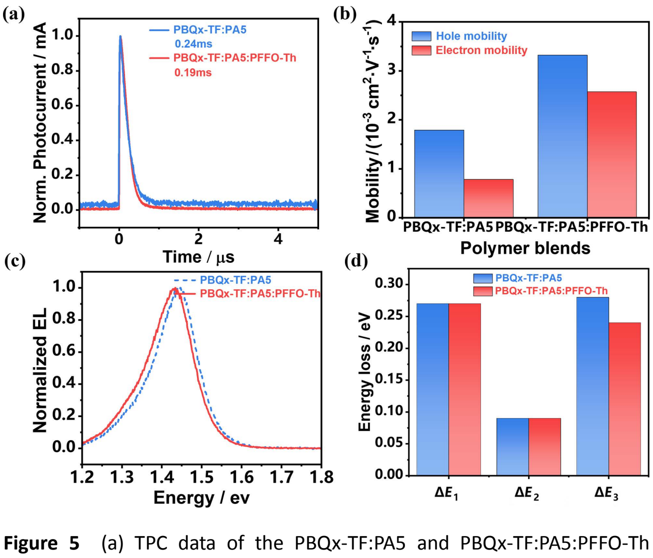

Figure 5 (a) TPC data of the PBQx-TF:PA5 and PBQx-TF:PA5:PFFO-Th devices. (b) The hole and electron mobilities of the PBQx-TF:PA5 and PBQx-TF:PA5:PFFO-Th devices. (c) EL spectra of the PBQx-TF:PA5 and PBQx-TF:PA5:PFFO-Th devices. (d) ΔE_1, ΔE_2, and ΔE_3 values of the PBQx-TF:PA5 and PBQx-TF:PA5:PFFO-Th devices.

To determine the origin of the differing V_{OC} results in the two all-PSCs, we conducted measurements of the ΔE_{loss} by analyzing Fourier-transform photocurrent spectroscopy external quantum efficiency (FTPS-EQE) and electroluminescence (EL) spectra. Typically, the ΔE_{loss} is partitioned into three contributions: (1) radiative recombination loss above the bandgap (ΔE_1), (2) radiative recombination loss below the bandgap (ΔE_2), and (3) nonradiative recombination loss (ΔE_3), where $\Delta E_3 = -kT\ln(EQE_{EL})$. The electroluminescence and FTPS-EQE spectra for the binary and ternary devices are displayed in Figure 5c and Figure S5, respectively. The corresponding calculated loss terms are provided in Figure 5d and Table S11. Both all-PSCs demonstrate similar ΔE_1 values of 0.27 eV. The ΔE_2 values for the two devices were also comparable, measuring 0.091 eV and 0.088 eV. The primary distinction in E_{loss} among the three devices arises from the ΔE_3 values, which were 0.277 eV and 0.244 eV for the PBQx-TF:PA5 and PBQx-TF:PA5:PFFO-Th-based devices, respectively. Finally, the PBQx-TF:PA5:PFFO-Th device achieved E_{loss} values of 0.602 eV, which are lower than those of the binary system. From an energy loss perspective, incorporating the third component offers an effective approach to minimizing energy loss and enhancing V_{OC}. As evidenced by GIWAXS measurements, the ternary blend exhibited tighter lamellar stacking (reduced interlamellar spacing from 21.20 Å to 20.43 Å) and increased CCL, indicating improved molecular ordering. This enhanced crystallinity reduces trap states and defects, which are primary sources of non-radiative recombination. The more ordered structure facilitates efficient charge transport and minimizes carrier trapping, thereby suppressing non-radiative losses. Therefore, the addition of PFFO-Th reduces non-radiative recombination losses by optimizing the active layer's crystallinity, improving charge transport, passivating trap states, and facilitating efficient energy transfer. These synergistic effects collectively contribute to the enhanced device performance, particularly the higher V_{OC} and PCE observed in the ternary system.

As shown in Figure 6a, transient photovoltage (TPV) along with charge-extraction (CE) measurements were conducted across a range of light intensities, enabling simultaneous determination of carrier densities (n) and lifetimes (τ), for more thorough analysis of carrier recombination dynamics. At different light intensities, the PBQx-TF:PA5:PFFO-Th device demonstrates increased carrier density and extended carrier lifetime. Figure 6b illustrates the relationship between τ and n for the devices. Increased values of n and τ lead to ameliorative exciton dissociation and a depressed carrier recombination,[52] consistent with the observed improvement in J_{SC}. To further investigate bimolecular recombination in the two systems, the nongeminate recombination rate constant (k_{rec}) was calculated using the equation $k_{rec} = 1/[(\lambda + 1)n\tau]$, where λ represents the recombination order derived from Figure 6b, and shows a strong dependence on the values of n and τ. The relationship between k_{rec} and n is illustrated in Figure 6c. The k_{rec} value of the PBQx-TF:PA5:PFFO-Th device is greater than that of the PBQx-TF:PA5 devices across different light intensities. These findings indicate that the addition of PFFO-Th effectively suppresses bimolecular recombination in the PBQx-TF:PA5 blend film, leading to an enhanced J_{SC}. To gain deeper insight into the recombination loss of carriers, the trap density of states (DOS) within the PBQx-TF:PA5 and PBQx-TF:PA5:PFFO-Th devices was examined.

The distribution of trap DOS is determined using capacitance-frequency spectra. This measurement was conducted in the dark, with minimal alternating current voltage applied to ensure the devices to continuously capture and release carriers. The distribution of trap DOS, denoted as NT (E_ω), and the frequency (ω) adhere to relation

$$N_{\mathrm{T}}\ (E_\omega) = \frac{\beta}{qAd}\frac{V_{\mathrm{bi}}}{kT}\frac{\omega \mathrm{d}C}{\mathrm{d}\omega} \tag{1}$$

while the correlation between trap energy (E_ω) and ω is described by equation

$$E_\omega\ = kT\ln(\frac{\omega_{\ 0}}{\omega}) \tag{2}$$

in which the built-in potential is denoted by V_{bi}, while ω_0 represents the thermal excitation rate prefactor from trap states, typically assumed to be 10^{12} s^{-1} based on previous studies. The correction factor β is assigned a unit value in this investigation, and A corresponds to the device's active area, representing the actual working surface of the photovoltaic structure. The built-in potential (V_{bi}) was determined through capacitance-voltage (C-V) characterization. This measurement technique involves plotting C^{-2} against applied voltage, where the linear region at lower voltages intersects the voltage axis, indicating the V_{bi} value. Analysis revealed distinct built-in potentials for the different device configurations: 0.92 V for PBQx-TF:PA5:PFFO-Th and 0.97 V for PBQx-TF:PA5, with detailed data presented in Figure 6d and Table S12 (Supporting Information).

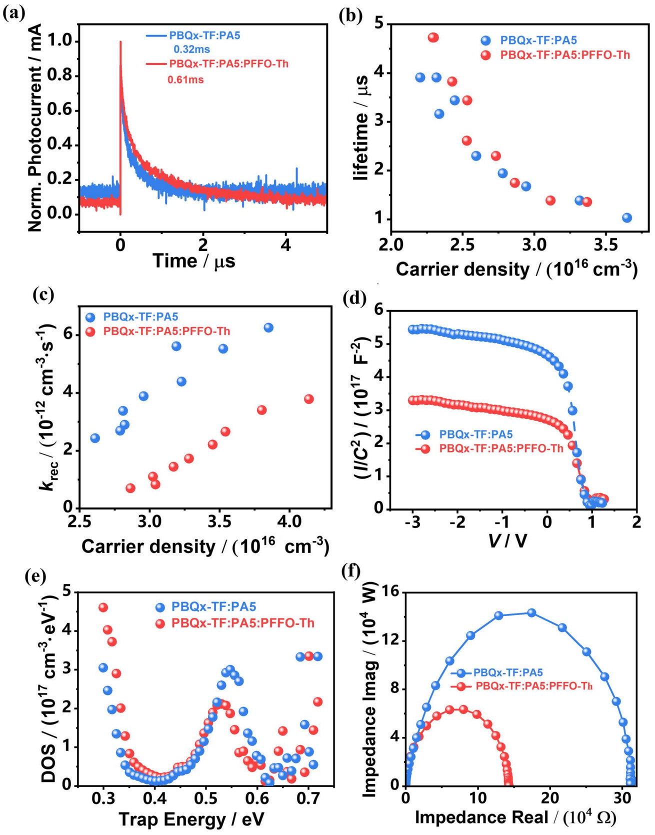

Figure 6 (a) TPV data of the PBQx-TF:PA5 and PBQx-TF:PA5:PFFO-Th devices. (b) Carrier lifetime versus carrier density of PBQx-TF:PA5 and PBQx-TF:PA5:PFFO-Th devices. (c) Bimolecular recombination rate constants (k_{rec}) versus carrier density of PBQx-TF:PA5 and PBQx-TF:PA5:PFFO-Th devices. (d) C-V curves for the PBQx-TF:PA5 and PBQx-TF:PA5:PFFO-Th devices to obtain V_{bi}. e) Trap density of states of PBQx-TF:PA5 and PBQx-TF:PA5:PFFO-Th devices. (f) Equivalent circuit model and Nyquist plots for PBQx-TF:PA5 and PBQx-TF:PA5:PFFO-Th devices.

Reduced trap state density and shallower energy levels within the band gap significantly improve charge carrier dynamics. These favorable conditions promote more efficient charge transport while simultaneously decreasing recombination rates and minimizing photocurrent losses in the photovoltaic system. While all three all-PSC devices exhibit comparable trap state energy distributions, the PBQx-TF:PA5:PFFO-Th configuration demonstrates a significantly reduced trap DOS at 2.17×10^{17} cm^{-3}, representing a notable decrease compared to the PBQx-TF:PA5 system's 2.99×10^{17} cm^{-3}. This reduction in trap DOS contributes to enhanced device performance by minimizing recombination losses and enabling increased photocurrent generation, as evidenced in Figure 6e.

To better understand charge transport dynamics and recombination mechanisms, electrochemical impedance spectroscopy (EIS) analysis was conducted, for providing valuable insights into the fundamental processes governing charge behavior within the system. Impedance measurements were conducted on all-PSC devices under dark conditions, with an applied bias voltage matching their V_{OC}. The resulting data were represented as Nyquist plots for detailed analysis of the devices' electrical characteristics. The Nyquist plot analysis employed an equivalent circuit model incorporating two parallel resistance-capacitance elements, as illustrated in Figure 6f. Detailed fitting parameters for this model are provided in Tables S13 and S14 (Supporting Information). Within this electrical representation, the R_1 component corresponds to the cumulative series resistance originating from various device interfaces and electrode materials, specifically ITO, PEDOT:PSS, PNDIT-$\mathrm{F_3}$N-Br, and Ag. In the equivalent circuit model, the first parallel resistance-capacitance element (R_1) accounts for the cumulative series resistance arising from electrode materials and interfacial components, specifically ITO, PEDOT:PSS, PNDIT-$\mathrm{F_3}$N-Br, and Ag. The second element (R_2-C_2) characterizes the electrical behavior of the active layer, while the third element (R_3-C_3) describes the interfacial electrical properties at two critical junctions: the PEDOT:PSS/active layer interface and the active layer/PNDIT-$\mathrm{F_3}$N-Br interface. Analysis of the electrical characteristics reveals comparable interface resistances across all three LBL devices. Notably, the PBQx-TF:PA5:PFFO-Th composite film demonstrates significantly lower bulk resistance (121 Ω) compared to the PBQx-TF:PA5 system (290 Ω), representing an approximately 50% reduction. This substantial decrease in bulk resistance facilitates improved charge carrier mobility while effectively minimizing recombination losses within the photovoltaic structure.

Conclusions

In this study, we explored the impact of introducing the PFFO-Th polymer as the third component into PBQx-TF: PA5 binary system for constructing ternary all-PSCs. The incorporation of PFFO-Th resulted in a notable improvement in device performance, achieving a power conversion efficiency (PCE) of 18.55%, compared to 16.69% for the binary counterpart. This enhancement was primarily attributed to the synergistic effects of energy level alignment, optimized morphology, and efficient charge transport. From a theoretical perspective, the addition of PFFO-Th formed a LUMO energy cascade across PBQx-TF, PFFO-Th, and PA5, facilitating exciton dissociation and reducing recombination losses. This was further supported by the improved crystallization and tighter lamellar stacking observed in GIWAXS measurements. The enhanced face-on orientation and elongated fibril morphology in the ternary blend provided more efficient charge transport pathways. Additionally, transient photovoltage and charge-extraction measurements confirmed that the ternary device exhibited longer carrier lifetimes, and suppressed bimolecular recombination rates. The reduction in energy loss, particularly nonradiative recombination loss (ΔE_3), highlighted the role of PFFO–Th in lowering energy loss and improving the V_{OC}. Photoluminescence (PL) and Förster resonance energy transfer (FRET) analyses indicated that PFFO-Th not only assisted in exciton dissociation but also acted as an intermediary for energy transfer between PBQx-TF and PA5. The use of non-halogenated solvents in our ternary system is highly advantageous for large-scale, roll-to-roll (R2R) processing since the fabrication process will be more environmentally friendly for industrial use, which is critical for scaling up production. The compatibility of PFFO-Th with the binary system, along with its ability to improve film morphology and charge transport, suggests that the ternary blend can be potentially adapted to R2R manufacturing techniques. Overall, this study demonstrates that incorporating PFFO-Th into the active layer optimizes the physical, electronic, and morphological properties of the ternary all-PSC, paving the way for designing high-performance photovoltaic devices with reduced energy losses and efficient charge dynamics.

Experimental

Device fabrication: The PBQx-TF:PA5:PFFO-Th blends (weight ratios are 1 : 0.9 : 0.1), were dissolved in *o*-xylene (the concentration of donor was 5.5 mg·mL^{-1} for all blends), with 2-methylnaphthalene (1% vol) as additive, and stirred at 120 °C hotplate for 2 h. The blend solution was spin-coated at around 3300 r/min for 60 s onto PEDOT:PSS film followed by a temperature annealing of 100 °C for 10 min. The thickness of the optimized devices is around 100—110 nm. Afterwards, 5 nm PNDIT-F$_3$N-Br was spin-coated onto the active layers as a cathode interface. Finally, 100 nm silver was thermally deposited on top of the interface through a shadow mask in a vacuum chamber at a pressure of 1 × 10^{-7} mbar. The effective area of the device was confined to 0.04 cm^2 by a non-refractive mask to improve the accuracy of measurements.

Other characterization details including CV and morphology measurement are provided in Supporting Information.

Supporting Information

The supporting information for this article is available on the WWW under https://doi.org/10.1002/cjoc.70075.

Acknowledgement

This work was financially supported by Guangdong Natural Science Foundation (No. 2021B1515120073), the Guangdong Provincial Science and Technology Foundation (No. 2022A0505050068), the Jiangxi Provincial Natural Science Foundation (No. 20224BAB204033), Hubei Provincial Natural Science Foundation of China (2024AFB950), and Excellent Discipline Cultivation Project by JHUN (2023XKZ031). R. Ma acknowledges the support from PolyU Distinguished Postdoctoral Fellowship (1-YW4C).

References

[1] Lee, C.; Lee, S.; Kim, G.-U.; Lee, W.; Kim, B. J. Recent Advances, Design Guidelines, and Prospects of All-Polymer Solar Cells. *Chem. Rev.* **2019**, *119*, 8028–8086.

[2] Zhang, Z.-G.; Li, Y. Polymerized Small-Molecule Acceptors for High-Performance All-Polymer Solar Cells. *Angew. Chem. Int. Ed.* **2021**, *60*, 4422–4433.

[3] Bai, H.; Fan, Q.; Ma, R.; Guo, X.; Ma, W.; Zhang, M. Non-Fully Conjugated Photovoltaic Materials with Y-Series Acceptor Backbone for High-Performance Organic Solar Cells. *Chin. J. Chem.* **2024**, *42*, 1307–1318.

[4] Pankow, R. M.; Wu, J.; Harbuzaru, A.; Kerwin, B.; Chen, Y.; Ortiz, R. P.; Facchetti, A.; Marks, T. J. All-Polymer Solar Cells Incorporating Readily Accessible Naphthalene Diimide and Isoindigo Acceptor Polymers for Improved Light Harvesting. *Chem. Mater.* **2022**, *34*, 3267–3279.

[5] Ma, R.; Fan, Q.; Dela Peña, T. A.; Wu, B.; Liu, H.; Wu, Q.; Wei, Q.; Wu, J.; Lu, X.; Li, M.; Ma, W.; Li, G. Unveiling the Morphological and Physical Mechanism of Burn-in Loss Alleviation by Ternary Matrix toward Stable and Efficient All-Polymer Solar Cells. *Adv. Mater.* **2023**, *35*, 2212275.

[6] Wang, Z.; Wang, X.; Tu, L.; Wang, H.; Du, M.; Dai, T.; Guo, Q.; Shi, Y.; Zhou, E. Dithienoquinoxalineimide-Based Polymer Donor Enables All-Polymer Solar Cells Over 19 % Efficiency. *Angew. Chem. Int. Ed.* **2024**, *63*, e202319755.

[7] Meng, Y.; L, Tang; Xiao, M.; Zhou, W.; Li, N.; Jia, J.; Jia, T.; Su, W.; Bi, Z.; Peng, W.; Fan, B.; Jen, A. K. Y.; Ma, W.; Fan, Q. Efficient All-Polymer Solar Cells Enabled by a Novel Medium Bandgap Guest Acceptor. *Chin. J. Chem.* **2024**, *42*, 3559–3566.

[8] Zhang, C.; Song, A.; Huang, Q.; Cao, Y.; Zhong, Z.; Liang, Y.; Zhang, K.; Liu, C.; Huang, F.; Cao, Y. All-Polymer Solar Cells and Photodetectors with Improved Stability Enabled by Terpolymers Containing Antioxidant Side Chains. *Nano-Micro Lett.* **2023**, *15*, 140.

[9] Wang, T.; Chen, M.; Sun, R.; Min, J. Recent research progress of all-polymer solar cells based on PSMA-type polymer acceptors. *Chem* **2023**, *9*, 1702–1767.

[10] Ma, R.; Li, H.; Dela Peña, T. A.; Xie, X.; Fong, P. W.-K.; Wei, Q.; Yan, C.; Wu, J.; Cheng, P.; Li, M.; Li, G. Tunable Donor Aggregation Dominance in a Ternary Matrix of All-Polymer Blends with Improved Efficiency and Stability. *Adv. Mater.* **2024**, *36*, 2304632.

[11] Li, H.; Le, J.; Tan, H.; Hu, L.; Li, X.; Zhang, K.; Zeng, S.; Liu, Q.; Zhang, M.; Shi, L.; Cai, Z.; Liu, S.; Li, H.; Ye, L.; Hu, X.; Chen, Y. Synergistic Multimodal Energy Dissipation Enhances Certified Efficiency of Flexible Organic Photovoltaics beyond 19%. *Adv. Mater.* **2025**, *37*, 2411989.

[12] Wu, X.; Xiao, B.; Sun, R.; Yang, X.; Zhang, M.; Gao, Y.; Xiao, B.; Papkovskaya, E. D.; Luponosov, Y.; Brabec, C. J.; Min, J. 19.46%-Efficiency all-polymer organic solar cells with excellent outdoor operating stability enabled by active layer reconstruction. *Energy Environ. Sci.* **2025**, *18*, 1812–1823.

[13] An, M.; Liu, Q.; Jeong, S. Y.; Liu, B.; Huang, E.; Liang, Q.; Li, H.; Zhang, G.; Woo, H. Y.; Niu, L.; Guo, X.; Sun, H. A Fluorinated Imide-Functionalized Arene Enabling a Wide Bandgap Polymer Donor for Record-Efficiency All-Polymer Solar Cells. *Angew. Chem. Int. Ed.* **2024**, *63*, e202410498.

[14] Wang, J.; Li, Y.; Han, C.; Chen, L.; Bi, F.; Hu, Z.; Yang, C.; Bao, X.; Chu, J. All-polymer solar cells with 19% efficiency via introducing pincer-shaped non-covalent bond interactions. *Energy Environ. Sci.* **2024**, *17*, 4216–4227.

[15] Wang, J.; Wang, Y.; Xian, K.; Qiao, J.; Chen, Z.; Bi, P.; Zhang, T.; Zheng, Z.; Hao, X.; Ye, L.; Zhang, S.; Hou, J. Regulating Phase Separation Kinetics for High-Efficiency and Mechanically Robust All-Polymer Solar Cells. *Adv. Mater.* **2024**, *36*, 2305424.

[16] Guo, J.; Xia, X.; Qiu, B.; Zhang, J.; Qin, S.; Li, X.; Lai, W.; Lu, X.; Meng, L.; Zhang, Z.; Li, Y. Manipulating Polymer Backbone Configuration via Halogenated Asymmetric End-Groups Enables Over 18% Efficiency All-Polymer Solar Cells. *Adv. Mater.* **2023**, *35*, 2211296.

[17] Ma, S.; Li, H.; Wu, W.; Gámez-Valenzuela, S.; Ma, R.; Bai, Q.; Zhong, J.; Jeong, S. Y.; Liu, Q.; Zhang, H.; Zhang, G.; Zhang, W.; Chen, J.; Huang, E.; Liu, B.; Feng, K.; Woo, H. Y.; Niu, L.; Sun, H.; Guo, X. Chlorinated Bithiophene Imide-Based n-Type Polymers: Synthesis, Structure–Property Correlations, and Applications in Organic Electronic Devices. *Angew. Chem. Int. Ed.* **2025**, *64*, e202423616.

[18] Bai, H.; Fan, Q.; Ma, R.; Guo, X.; Ma, W.; Zhang, M. Non-Fully Conjugated Photovoltaic Materials with Y-Series Acceptor Backbone for High-Performance Organic Solar Cells. *Chin. J. Chem.* **2024**, *42*, 1307–1318.

[19] Günther, M.; Kazerouni, N.; Blätte, D.; Perea, J. D.; Thompson, B. C.; Ameri, T. Models and mechanisms of ternary organic solar cells. *Nat. Rev. Mater.* **2023**, *8*, 456–471.

[20] Ge, Z.; Qiao, J.; Li, Y.; Song, J.; Duan, X.; Fu, Z.; Hu, H.; Yang, R.; Yin, H.; Hao, X.; Sun, Y. Regulating Electron-Phonon Coupling by Solid Additive for Efficient Organic Solar Cells. *Angew. Chem. Int. Ed.* **2025**, *64*, e202413309.

[21] Jiang, Y.; Sun, S.; Xu, R.; Liu, F.; Miao, X.; Ran, G.; Liu, K.; Yi, Y.; Zhang, W.; Zhu, X. Non-fullerene acceptor with asymmetric structure and

phenyl-substituted alkyl side chain for 20.2% efficiency organic solar cells. *Nat. Energy* **2024**, *9*, 975–986.

[22] Chen, H.; Huang, Y.; Zhang, R.; Mou, H.; Ding, J.; Zhou, J.; Wang, Z.; Li, H.; Chen, W.; Zhu, J.; Cheng, Q.; Gu, H.; Wu, X.; Zhang, T.; Wang, Y.; Zhu, H.; Xie, Z.; Gao, F.; Li, Y.; Li, Y. Organic solar cells with 20.82% efficiency and high tolerance of active layer thickness through crystallization sequence manipulation. *Nat. Mater.* **2025**, *24*, 444–453.

[23] Luo, Z.; Wei, W.; Ma, R.; Ran, G.; Jee, M. H.; Chen, Z.; Li, Y.; Zhang, W.; Woo, H. Y.; Yang, C. Approaching 20% Efficiency in *ortho*-Xylene Processed Organic Solar Cells by a Benzo[a]phenazine-Core-Based 3D Network Acceptor with Large Electronic Coupling and Long Exciton Diffusion Length. *Adv. Mater.* **2024**, *36*, 2407517.

[24] Wei, N.; Chen, J.; Cheng, Y.; Bian, Z.; Liu, W.; Song, H.; Guo, Y.; Zhang, W.; Liu, Y.; Lu, H.; Zhou, J.; Bo, Z. Constructing Multiscale Fibrous Morphology to Achieve 20% Efficiency Organic Solar Cells by Mixing High and Low Molecular Weight D18. *Adv. Mater.* **2024**, *36*, 2408934.

[25] Gu, X.; Wei, Y.; Zeng, R.; Lv, J.; Hou, Y.; Yu, N.; Tan, S.; Wang, Z.; Li, C.; Tang, Z.; Peng, Q.; Liu, F.; Cai, Y.; Zhang, X.; Huang, H. Suppressing Exciton–Vibration Coupling via Intramolecular Noncovalent Interactions for Low-Energy-Loss Organic Solar Cells. *Angew. Chem. Int. Ed.* **2025**, *64*, e202418926.

[26] Ma, R.; Li, H.; Dela Peña, T. A.; Wang, H.; Yan, C.; Cheng, P.; Wu, J.; Li, G. *In-situ* understanding on the formation of fibrillar morphology in green solvent processed all-polymer solar cells. *Nat. Sci. Rev.* **2024**, *11*, nwae384.

[27] Guan, S.; Li, Y.; Bi, Z.; Lin, Y.; Fu, Y.; Wang, K.; Wang, M.; Ma, W.; Xia, J.; Ma, Z.; Tang, Z.; Lu, X.; Zuo, L.; Li, H.; Chen, H. Fine-tuning the hierarchical morphology of multi-component organic photovoltaics via a dual-additive strategy for 20.5% efficiency. *Energy Environ. Sci.* **2025**, *18*, 313–321.

[28] Fan, B.; Gao, H.; Yu, L.; Li, R.; Wang, L.; Zhong, W.; Wang, Y.; Jiang, W.; Fu, H.; Chen, T.; Kan, B.; Tsang, S.-W.; Jen, A. K. Y. Local Structure-Induced Selective Interactions Enables High-Performance and Burn-in-Free Organic Photovoltaics. *Angew. Chem. Int. Ed.* **2025**, *64*, e202418439.

[29] Sun, Y.; Wang, L.; Guo, C.; Xiao, J.; Liu, C.; Chen, C.; Xia, W.; Gan, Z.; Cheng, J.; Zhou, J.; Chen, Z.; Zhou, J.; Liu, D.; Wang, T.; Li, W. π-Extended Nonfullerene Acceptor for Compressed Molecular Packing in Organic Solar Cells To Achieve over 20% Efficiency. *J. Am. Chem. Soc.* **2024**, *146*, 12011–12019.

[30] Chen, Z.; Ge, J.; Song, W.; Tong, X.; Liu, H.; Yu, X.; Li, J.; Shi, J.; Xie, L.; Han, C.; Liu, Q.; Ge, Z. 20.2% Efficiency Organic Photovoltaics Employing a π-Extension Quinoxaline-Based Acceptor with Ordered Arrangement. *Adv. Mater.* **2024**, *36*, 2406690.

[31] Wang, Y.; Sun, K.; Li, C.; Zhao, C.; Gao, C.; Zhu, L.; Bai, Q.; Xie, C.; You, P.; Lv, J.; Sun, X.; Hu, H.; Wang, Z.; Hu, H.; Tang, Z.; He, B.; Qiu, M.; Li, S.; Zhang, G. A Novel Upside-Down Thermal Annealing Method Toward High-Quality Active Layers Enables Organic Solar Cells with Efficiency Approaching 20%. *Adv. Mater.* **2024**, *36*, 2411957.

[32] Bin, H.; Zhang, P.; Gao, N.; Du, B.; Xu, Z.; Wu, S.; Zhu, K.; Ma, X.; Li, Y. Highly Ordered Polymorphism of Small Molecule Acceptor Delivering Efficient and Stable Binary Organic Solar Cells. *Angew. Chem. Int. Ed.* **2025**, *64*, e202424430.

[33] Ling, Z.; Wu, J.; Jurado, J. P.; Petoukhoff, C. E.; Jeong, S. Y.; Naphade, D.; Babics, M.; Chang, X.; Faber, H.; Doukas, S.; Lidorikis, E.; Nugraha, M. I.; He, M.; Alqurashi, M.; Lin, Y.; Sun, X.; Hu, H.; Woo, H. Y.; De Wolf, S.; Tsetseris, L.; Laquai, F.; Yu, D.; Wang, E.; Anthopoulos, T. D. 20.5% efficient ternary organic photovoltaics using an asymmetric small-molecular acceptor to manipulate intermolecular packing and reduce energy losses. *Mater. Sci. Eng. R Rep.* **2025**, *163*, 100922.

[34] Wang, J.; Wang, P.; Chen, T.; Zhao, W.; Wang, J.; Lan, B.; Feng, W.; Liu, H.; Liu, Y.; Wan, X.; Long, G.; Kan, B.; Chen, Y. Isomerism Effect of 3D Dimeric Acceptors for Non-Halogenated Solvent-Processed Organic Solar Cells with 20 % Efficiency. *Angew. Chem. Int. Ed.* **2025**, *64*, e202423562.

[35] Zhou, K.; Han, D.; Xian, K.; Li, S.; Gao, M.; Zhang, K.; Zhao, B.; Li, X.; Chen, Y.; Geng, Y.; Ye, L. Simultaneously improved stretchability, stability, and output power in solar cells via entanglement control. *Energy Environ. Sci.* **2024**, *17*, 5950–5961.

[36] Wang, Y.; Yu, J.; Zhang, R.; Yuan, J.; Hultmark, S.; Johnson, C. E.; Gallop, N. P.; Siegmund, B.; Qian, D.; Zhang, H.; Zou, Y.; Kemerink, M.; Bakulin, A. A.; Müller, C.; Vandewal, K.; Chen, X.-K.; Gao, F. Origins of the open-circuit voltage in ternary organic solar cells and design rules for minimized voltage losses. *Nat. Energy* **2023**, *8*, 978–988.

[37] Yang, X.; Sun, R.; Wang, Y.; Chen, M.; Xia, X.; Lu, X.; Lu, G.; Min, J. Ternary All-Polymer Solar Cells with Efficiency up to 18.14% Employing a Two-Step Sequential Deposition. *Adv. Mater.* **2023**, *35*, 2209350.

[38] Xu, W.; Tian, H.; Ni, Y.; Xu, Y.; Zhang, L.; Zhang, F.; Wu, S.; Young Jeong, S.; Huang, T.; Du, X.; Li, X.; Ma, Z.; Young Woo, H.; Zhang, J.; Ma, X.; Wang, J.; Zhang, F. Eco-friendly solvent-processed layer-by-layer ternary all-polymer solar cells exhibiting over 18.5% efficiency. *Chem. Eng. J.* **2024**, *493*, 152558.

[39] Zhang, J.; Zhou, Q.; Xie, J.; Zhao, J.; Yu, J.; Zhang, K.; Jia, T.; Huang, F.; Cao, Y. Ternary Strategy Enables Non-Halogenated Solvent-Processed All-Polymer Solar Cells with High Efficiency Over 18%. *Adv. Funct. Mater.* **2024**, *34*, 2313722.

[40] Lee, J.-W.; Kim, J.; Nguyen, T. H.-Q.; Lee, D. C.; Tan, Z.; Park, J.; Phan, T. N.-L.; Cho, S.; Kim, B. J. High efficiency and thermally stable ternary all-polymer solar cells achieved by alloyed vinyl-linked polymerized small-molecule acceptors. *Nano Energy* **2024**, *122*, 109338.

[41] Jia, T.; Zhang, J.; Zhang, G.; Liu, C.; Tang, H.; Zhang, K.; Huang, F. Rationally regulating the terminal unit and copolymerization spacer of polymerized small-molecule acceptors for all-polymer solar cells with high open-circuit voltage over 1.10 V. *J. Mater. Chem. A* **2022**, *10*, 15932–15940.

[42] Zhang, T.; Xu, Y.; Yao, H.; Zhang, J.; Bi, P.; Chen, Z.; Wang, J.; Cui, Y.; Ma, L.; Xian, K.; Li, Z.; Hao, X.; Wei, Z.; Hou, J. Suppressing the energetic disorder of all-polymer solar cells enables over 18% efficiency. *Energy Environ. Sci.* **2023**, *16*, 1581–1589.

[43] Jia, J.; Huang, Q.; Jia, T.; Zhang, K.; Zhang, J.; Miao, J.; Huang, F.; Yang, C. Fine-Tuning Batch Factors of Polymer Acceptors Enables a Binary All-Polymer Solar Cell with High Efficiency of 16.11%. *Adv. Energy Mater.* **2022**, *12*, 2103193.

[44] Tian, H.; Luo, Y.; Chen, Z.; Xu, T.; Ma, R.; Wu, J.; Li, G.; Yang, C.; Luo, Z. Improving Molecular Arrangement and Alleviating Nonradiative Energy Loss Using a Chlorinated Pyrido[3,4-*b*] Quinoxaline-Core-Based Acceptor for High-Performance Organic Solar Cells. *Adv. Energy Mater.* **2025**, *15*, 2404537.

[45] Ma, R.; Jiang, X.; Dela Peña, T. A.; Gao, W.; Wu, J.; Li, M.; Roth, S. V.; Müller-Buschbaum, P.; Li, G. Insulator Polymer Matrix Construction on All-Small-Molecule Photoactive Blend Towards Extrapolated 15000 Hour T_{80} Stable Devices. *Adv. Mater.* **2024**, *36*, 2405005.

[46] Jung, S.; Yang, U. J.; Oh, J.; Jeong, S.; Cho, Y.; Lee, G. H.; Choi, M. K.; Yang, C. Transfer Printing of Photoactive Layer Enabling Efficient, Wearable, and Dual-Function Organic Solar Cell Modules for a Wireless Healthcare Monitoring System. *Adv. Funct. Mater.* **2024**, *34*, 2406200.

[47] Jiang, X.; Gillett, A. J.; Zheng, T.; Song, X.; Heger, J. E.; Sun, K.; Spanier, L. V.; Guo, R.; Liang, S.; Bernstorff, S.; Müller-Buschbaum, P. Operando study of the influence of small molecule acceptors on the morphology induced device degradation of organic solar cells with different degrees of π–π stacking. *Energy Environ. Sci.* **2023**, *16*, 5970–5981.

[48] Rivnay, J.; Mannsfeld, S. C. B.; Miller, C. E.; Salleo, A.; Toney, M. F. Quantitative Determination of Organic Semiconductor Microstructure from the Molecular to Device Scale. *Chem. Rev.* **2012**, *112*, 5488–5519.

[49] Khasbaatar, A.; Damron, A. M.; Fernando, P. S.; Williams, J. S.; Zhu, C.; Gann, E. H.; Lee, J.-H.; Birge, A.; Kim, B.; Sabury, S.; Lee, M. L.; Reynolds, J. R.; Diao, Y. Lyotropic Liquid Crystal Mediated Assembly of Donor Polymers Enhances Efficiency and Stability of Blade-Coated Organic Solar Cells. *Adv. Mater.* **2025**, *37*, 2414632.

[50] Peng, Z.; Ye, L.; Ade, H. Understanding, quantifying, and controlling the molecular ordering of semiconducting polymers: from novices to experts and amorphous to perfect crystals. *Mater. Horiz.* **2022**, *9*,

577–606.

[51] Dela Peña, T. A.; Ma, R.; Xing, Z.; Wei, Q.; Khan, J. I.; Young, R. M.; Hai, Y.; Garcia, S. A.; Zou, X.; Jin, Z.; Ng, F. L.; Yeung, K. L.; Swearer, D. F.; Wasielewski, M. R.; Wang, J.; Cha, H.; Yan, H.; Wong, K. S.; Li, G.; Li, M.; Wu, J. Interface property–functionality interplay suppresses bimolecular recombination facilitating above 18% efficiency organic solar cells embracing simplistic fabrication. *Energy Environ. Sci.* **2023**, *16*, 3416–3429.

[52] Firdaus, Y.; Maffei, L. P.; Cruciani, F.; Müller, M. A.; Liu, S.; Lopatin, S.; Wehbe, N.; Ndjawa, G. O. N.; Amassian, A.; Laquai, F.; Beaujuge, P. M. Polymer Main-Chain Substitution Effects on the Efficiency of Non-fullerene BHJ Solar Cells. *Adv. Energy Mater.* **2017**, *7*, 1700834.

Manuscript received: March 6, 2025
Manuscript revised: April 9, 2025
Manuscript accepted: April 18, 2025
Version of record online: May 29, 2025

The Authors

Left to Right: (Top row) Rouren Chen, Tianyi Zhang, Qiqing Ruan, Lunbi Wu, Zhixuan Xu, (Middle row) Yuan Su, Zhixiong Cao, Qingduan Li, Biao Xiao, Ruijie Ma, (Bottom row) Yue-peng Cai, Tao Jia, Shengjian Liu, Gang Li